


Large unconventional anomalous Hall effect arising from spin chirality within domain walls of an antiferromagnet EuZn_2Sb_2

Karan Singh , Orest Pavlosiuk , Shovan Dan , Dariusz Kaczorowski , and Piotr Wiśniewski *

Institute of Low Temperature and Structure Research, Polish Academy of Sciences, Okólna 2, 50-422 Wrocław, Poland

 (Received 6 August 2023; revised 3 February 2024; accepted 5 February 2024; published 6 March 2024)

The unconventional anomalous Hall effect was observed in the antiferromagnetic state of EuZn_2Sb_2 . Scaling of unconventional Hall conductivity with the longitudinal conductivity, and the magnitude of the Hall angle indicate spin chirality despite a collinear magnetic structure. Anomalies in magnetoresistance culminate in the same fields, in which the unconventional anomalous Hall resistance has maxima. The monotonous decrease of their magnitude with increasing temperature belittles the role of spin fluctuations here, which are important in isostructural compounds. These observations point to a prominent role of scalar spin chirality within domain walls, when the magnetic field tilts the Eu moments. Simple calculation of such spin chirality shows it is strongest in fields that are characteristic for anomalous magnetotransport.

DOI: [10.1103/PhysRevB.109.125107](https://doi.org/10.1103/PhysRevB.109.125107)

I. INTRODUCTION

In several Eu-based antiferromagnets from the 1:2:2 family of pnictides, e.g., EuCd_2As_2 , EuCd_2Sb_2 , and EuZn_2As_2 , unconventional contributions to the anomalous Hall effect (AHE) have recently been reported [1–5]. The origin of those contributions is still not understood well enough. Interestingly, EuCd_2Sb_2 and EuCd_2As_2 are Weyl semimetals [1,6,7], while EuZn_2As_2 has the Fermi level within a narrow (≈ 0.1 eV) gap and a flat band above it [4]. Spin-orbit coupling (SOC) decreases along the series: EuCd_2Sb_2 , EuCd_2As_2 , EuZn_2Sb_2 , and EuZn_2As_2 , whereas the appearance of topological band crossings depends on the relative strength of the SOC [1]. It seems, however, that the difference in electronic structures induced by SOC does not significantly affect the unconventional part of the anomalous Hall effect in this series, as both boundary materials, EuCd_2Sb_2 and EuZn_2As_2 , exhibit pronounced unconventional AHE [1,4]. The common features of the four above-mentioned materials are CaAl_2Si_2 -type crystal structure ($P\bar{3}m1$ space group), fairly close Néel temperatures, $T_N = 9.5, 7.4, 13.3,$ and 19.6 K, respectively, and, most likely, the same *A*-type antiferromagnetic (AFM) structure, with magnetic moments of Eu^{2+} ions ferromagnetically aligned within the *ab* planes, which are stacked antiferromagnetically along the *c* axis [4,8]. The application of a magnetic field \mathbf{H} leads to the canting of spins and their gradual alignment with the field direction, turning the collinear magnetic structure into a noncollinear one and, above certain, sufficiently strong field H_{sat} , into the fully spin-polarized state [6,8–10]. In contrast to isostructural 1:2:2 Eu-bearing compounds, the magnetoresistance and Hall effect data for EuZn_2Sb_2 have not been hitherto reported. The unconventional AHE is widespread in this family; however, its origin remained unclear because

the collinearity of the common antiferromagnetic structure seemed to exclude scalar or vector spin chirality. This gap motivated our work on high-quality single crystals of EuZn_2Sb_2 , aiming to determine the origin of the above-mentioned anomalies.

In magnetized materials, the Hall resistivity comprises an AHE contribution, proportional to the magnetization (M) [11,12]. Two mechanisms can be responsible for AHE: an extrinsic one, related to the scattering on impurities, and the intrinsic one, related to the momentum-space Berry curvature [13,14]. Enhanced Berry curvature induces strong AHE and can be generated in Bloch electronic bands, when inversion symmetry or time-reversal symmetry is broken and SOC is considerably strong [13,15]. The AHE induced by the intrinsic mechanism, related to the Berry curvature, has been proposed for several materials, including, e.g., HgCr_2Se_4 , Fe_5Sn_2 , and $\text{Co}_3\text{Sn}_2\text{S}_2$ [15–17]. Significant real-space Berry curvature can occur in systems with noncoplanar spin textures, in which the so-called topological Hall effect (THE) arises due to finite scalar spin chirality defined for any three neighboring spins, \mathbf{S}_i ($i = 1, 2, 3$), as $\chi_{ijk} = \mathbf{S}_i \cdot (\mathbf{S}_j \times \mathbf{S}_k)$ [12,18,19]. Such THE has been observed in helimagnets, e.g., MnSi and MnGe [20,21].

In antiferromagnets with collinear magnetic moments, there is neither net magnetization nor spin chirality; therefore, both AHE and THE are zero. On the other hand, several antiferromagnets with noncollinear spin structures, e.g., Mn_5Si_3 and Mn_3Ir , demonstrate large AHE [22,23]. In such antiferromagnets, an additional contribution to the ordinary Hall effect may alternatively be attributed to finite vector spin chirality, $\vec{\chi}_{ij} = (\mathbf{S}_i \times \mathbf{S}_j)$ [24], and also associated with the AFM domain walls [25].

Our key observations for EuZn_2Sb_2 are the large unconventional anomalous Hall effect, pronounced anomaly of magnetoresistance, and complex angular dependence of magnetoresistance. We propose that in an AFM-ordered state, all these effects stem from a common mechanism, due

*p.wisniewski@intibs.pl

predominantly to the scalar spin chirality occurring within domain walls in the applied magnetic field.

II. SAMPLE PREPARATION, CHARACTERIZATION, AND METHODS OF MEASUREMENTS

EuZn₂Sb₂ single crystals were grown from Sb flux by placing the starting composition, Eu:Zn:Sb, with a molar ratio of 1:2:45 in an alumina crucible. The crucible was sealed into an evacuated quartz ampule, heated up at a rate of 50 °C/h to 1000 °C, kept at this temperature for 20 h, and then cooled to 800 °C at a rate of 2 °C/h. Excess flux was removed by centrifugation. Energy-dispersive x-ray spectra (EDS) taken on a few pieces of the synthesized crystals showed the stoichiometry in a good agreement with the nominal composition (see Fig. S1(a) in the Supplemental Material [26]). The backscattering Laue diffraction (using Laue-COS, Proto Manufacturing) provided information on the crystal orientation and quality (see Fig. S1(b) in the Supplemental Material [26]). It also confirmed that EuZn₂Sb₂ crystallizes in the trigonal CaAl₂Si₂-type structure, with space group *P*3̄m1, as previously reported [9].

Magnetization was measured on an oriented single crystal using a SQUID magnetometer (MPMS-XL, Quantum Design). Electrical transport measurements were performed using the Physical Property Measurements System (PPMS-14 Quantum Design) with a conventional four-probe method. 50- μ m-thick silver wires were attached to a cuboid sample (cut from the oriented single crystals with a wire saw) with silver paint. An electric current of 1 mA was applied along the basal *ab* plane. The effect of misalignment of the contacts was eliminated by the symmetrization and antisymmetrization of longitudinal resistance and Hall resistance, respectively, recorded for opposite directions of applied magnetic field.

The characterization and basic physical properties of our samples (AFM with $T_N = 13.3$ K) presented in the Supplemental Material [26] (Figs. S2 and S3, for magnetic properties and heat capacity, respectively) are in perfect agreement with an earlier report [9]. The temperature dependence of the electrical resistivity, ρ_{xx} , that we measured in zero magnetic field (cf. Fig. S4 in the Supplemental Material [26]) is very similar to the metalliclike one reported by May *et al.* [27].

III. HALL EFFECT AND MAGNETORESISTANCE

We measured Hall resistivity (ρ_{xy}) at various temperatures in the 2–20 K range, with $\mathbf{j} \perp \mathbf{H} \parallel c$ [Fig. 1(a)]. The $M(H)$ isotherms for lowest temperatures [see Fig. 1(b)] show two regions of magnetic field, $H > H_{\text{sat}}$, where magnetic moments are fully polarized, and $H < H_{\text{sat}}$ range, in which the AFM component of the magnetic structure (staggered moment) is preserved. The $\rho_{xy}(H > H_{\text{sat}})$ is linear, thus it can be considered as a sum of the ordinary Hall resistivity, $\rho_{xy}^N = \mu_0 R_0 H$, and the conventional anomalous Hall resistivity, $\rho_{xy}^{\text{CA}} = R_S M$ (R_0 and R_S are the respective Hall coefficients). When $H < H_{\text{sat}}$, there occurs a pronounced nonlinear contribution to $\rho_{xy}(H)$. We ascribe it to the unconventional AHE, denoted as ρ_{xy}^{UA} , and propose that its origin is associated with the canted spin structure. Thus, $\rho_{xy}(H)$ consists of three terms [21]: $\rho_{xy} = \rho_{xy}^N + \rho_{xy}^{\text{CA}} + \rho_{xy}^{\text{UA}}$.

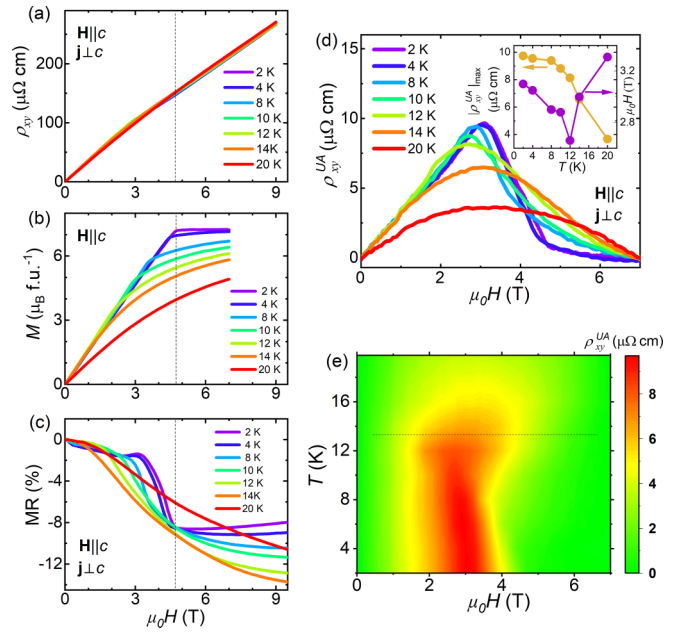


FIG. 1. Magnetic field dependence of (a) Hall resistivity, (b) magnetization, and (c) magnetoresistance. Dashed vertical lines in (a)–(c) mark the saturation field ($\mu_0 H_{\text{sat}} = 4.7$ T) at $T = 2$ K. (d) Unconventional anomalous Hall resistivity, ρ_{xy}^{UA} , as a function of the applied magnetic field, at several temperatures. Inset: Temperature dependence of ρ_{xy}^{UA} maxima (left axis) and magnetic field at which these maxima occur (right axis). (e) Map of ρ_{xy}^{UA} in the (H, T) plane (dotted horizontal line marks T_N).

A. Unconventional anomalous Hall resistivity

We decomposed the total $\rho_{xy}(H)$ by the following steps: (i) For $T = 2$ and 4 K, the ordinary component of Hall resistivity, $\rho_{xy}^N = R_0 \mu_0 H$, was estimated by linear fitting of $\rho_{xy}(H)$ in the 7–9 T range, and slopes of these fitted lines were taken as values of R_0 . For $T > 4$ K, R_0 was approximated as $\partial \rho_{xy} / \partial H$ for $\mu_0 H = 9$ T. So the estimated $R_0 \approx 28 \mu\Omega \text{ cm/T}$ barely changes with temperature (cf. Fig. S5(a) in the Supplemental Material [26]). (ii) This allowed us to calculate the sum of the anomalous components $(\rho_{xy}^{\text{CA}} + \rho_{xy}^{\text{UA}})(H)$, plotted in Fig. S5(b) of the Supplemental Material [26] for several temperatures in the 2–20 K range. At 2 K, $(\rho_{xy}^{\text{CA}} + \rho_{xy}^{\text{UA}})$ increases with increasing H , attains a maximum at $\mu_0 H \approx 2.8$ T, and then decreases to become nearly constant above 4.7 T. In the field of 7 T, all moments are aligned [cf. $M(H)$ in Fig. 1(b)], and $(\rho_{xy}^{\text{CA}} + \rho_{xy}^{\text{UA}})$ becomes field independent. (iii) Thus, we could neglect ρ_{xy}^{UA} and assume that $\rho_{xy}^{\text{CA}}(7 \text{ T}) = (\rho_{xy} - \rho_{xy}^N)$. The temperature dependence of the so-obtained ρ_{xy}^{CA} is shown in Fig. S5(c) in the Supplemental Material [26]. (iv) Next, we assumed that the R_S coefficient in $\rho_{xy}^{\text{CA}}(H)$ (usually proportional to ρ_{xx} [12]) is field independent at a given T (based on the practical independence of ρ_{xy}^{CA} from the field above H_{sat} and overall weak field dependence of ρ_{xx}). We used its values obtained for $\mu_0 H = 7$ T as $R_S = \rho_{xy}^{\text{CA}} / M(7 \text{ T})$ to calculate the unconventional term for $H < H_{\text{sat}}$, using the formula $\rho_{xy}^{\text{UA}}(H) = \rho_{xy} - \rho_{xy}^N(H) - R_S M(H)$. Obtained in this way, the $\rho_{xy}^{\text{UA}}(H)$ data for several different temperatures are plotted in Fig. 1(d). Below T_N , the $\rho_{xy}^{\text{UA}}(H)$ curves display

distinct maxima (e.g., in $\mu_0 H = 2.8$ T at $T = 2$ K). The maximum value of $9.8 \mu\Omega \text{ cm}$ is larger than reported: $\approx 0.2 \mu\Omega \text{ cm}$ for MnGe [21] or $\approx 2 \mu\Omega \text{ cm}$ for CoNb₃S₆ [28]. The $\rho_{xy}^{\text{UA}}(H)$ obtained for $T > T_N$ are distinctly different, which suggests another underlying mechanism, most likely due to spin fluctuations.

For our sample, as we show in the inset to Fig. 1(d), the maximum of $\rho_{xy}^{\text{UA}}(H)$ isotherm ($|\rho_{xy}^{\text{UA}}|_{\text{max}}$) decreases slightly with increasing temperature up to $\approx T_N$ and rapidly drops above this temperature. This is in contrast to other compounds in the 1:2:2 series having the largest $|\rho_{xy}^{\text{UA}}|_{\text{max}}$ at $T \approx T_N$, and indicates that the most important mechanism behind ρ_{xy}^{UA} in the AFM state of EuZn₂Sb₂ is the magnetic texture (which is most stable at lowest T), and also that two different mechanisms are responsible for ρ_{xy}^{UA} , with one of them active only at temperatures below T_N .

B. Comparison of unconventional anomalous Hall resistivity in isostructural compounds

The extrema of ρ_{xy}^{UA} in three isostructural compounds mentioned above span a vast range from -6 to $3 \times 10^5 \mu\Omega \text{ cm}$, and are strongly sample dependent [1–7]. In the case of EuCd₂As₂, the unconventional contribution has alternatively been ascribed to two different mechanisms, depending on Fermi energy (carrier concentration). Reported values of ρ_{xy} (at 2 K and 6 T, where anomalous contributions are negligible) depend on the sample, and vary from $35 \mu\Omega \text{ cm}$ [2] to $250 \mu\Omega \text{ cm}$ [3], corresponding to an over sevenfold decrease of hole concentration (n_h). In the former case (large Fermi energy), Berry curvature from Weyl points induced by fluctuating ferromagnetic domains was proposed as a driving force of ρ_{xy}^{UA} ; for the latter sample with small Fermi energy, the spin canting in the applied magnetic field was held responsible. Also, the maxima of ρ_{xy}^{UA} are sample dependent for EuCd₂As₂, spanning between $18 \mu\Omega \text{ cm}$ [2] and very large $380 \mu\Omega \text{ cm}$ [3].

Among the four discussed isostructural compounds, the strongest AHE is displayed by EuZn₂As₂, $\rho_{xy}^{\text{UA}} \cong 3 \times 10^5 \mu\Omega \text{ cm}$, and has been assigned to the short-range ferromagnetic order and canted magnetic moments, above and below T_N , respectively, resulting in nonzero spin chirality (those results have been obtained on a sample with extremely low, but strongly T -dependent $n_h = 3.1 \times 10^{15} \text{ cm}^{-3}$ at 2 K and $7.5 \times 10^{16} \text{ cm}^{-3}$ at 50 K) [5]. Another sample of the same compound, with T -independent $n_h = 8.6 \times 10^{17} \text{ cm}^{-3}$, showed a large $\rho_{xy}^{\text{UA}} \cong 500 \mu\Omega \text{ cm}$ [4]. For EuZn₂Sb₂ we found $n_h = 2.2 \times 10^{19} \text{ cm}^{-3}$, intermediate between the above-mentioned EuCd₂As₂ samples. On the other hand, EuCd₂Sb₂ shows very similar $n_h = 2.5 \times 10^{19} \text{ cm}^{-3}$, but its ρ_{xy}^{UA} is negative, having, at 2 K, a local extremum of $-6 \mu\Omega \text{ cm}$.

We summarized the above-described literature results in Table I and noticed that the magnitude of ρ_{xy}^{UA} is correlated with both the SOC and n_h . EuZn₂Sb₂ displays rather small ρ_{xy}^{UA} , most likely because of the rather weak effect of spin fluctuations. In order to compare it with that in EuCd₂As₂, we estimated an upper-limit temperature for a noticeable effect of spin fluctuations, $T_{\text{sf}} \approx 40$ K, from the behavior of the

TABLE I. The magnitudes of R_0 (obtained from ρ_{xy} in high fields, where the anomalous contribution is negligible), hole concentrations n_h resulting from those R_0 values, and extreme values of $\rho_{xy}^{\text{UA}}(H)$, through the series of four 1:2:2 compounds with decreasing strength of spin-orbit coupling (SOC) marked with a vertical arrow. All data, except those in the last row, were obtained at $T = 2$ K.

Compound	R_0 ($\Omega \text{ cm/T}$)	n_h (cm^{-3})	ρ_{xy}^{UA} ($\mu\Omega \text{ cm}$)	Ref.	SOC
EuCd ₂ Sb ₂	2.5×10^{-5}	2.5×10^{19}	-6	[1]	↓
EuCd ₂ As ₂	5.83×10^{-6}	1.1×10^{20}	18	[2]	
	7×10^{-4}	8.9×10^{17}	300	[7]	
	4.17×10^{-5}	1.5×10^{19}	380	[3]	
EuZn ₂ Sb ₂	2.8×10^{-5}	2.2×10^{19}	10	This work	
EuZn ₂ As ₂	7.5×10^{-4}	8.6×10^{17}	500	[4]	
	2×10^{-1}	3.1×10^{15}	$300\,000$	[5]	
$T = 50$ K	8.3×10^{-3}	7.5×10^{16}		[5]	

electrical resistivity, $\rho_{xx}(T)$, and magnetic susceptibility, $\chi(T)$, as shown in Fig. 2. We also calculated the relative increase of ρ_{xx} due to spin fluctuations, $\delta\rho_{xx} = \rho_{xx}(T_N)/\rho_{xx}(T_{\text{sf}}) - 1 = 0.016$. Corresponding values estimated from EuCd₂As₂ results shown in [2] are much larger: $\delta\rho_{xx} > 2$ and $T_{\text{sf}} \approx 100$ K. This implicates that spin fluctuations are much weaker, less abundant, and their effect on electrical resistivity is smaller in EuZn₂Sb₂ than in EuCd₂As₂. Nevertheless, they seem to induce the ρ_{xy}^{UA} we observed above T_N , similar to other compounds of the series.

C. Scaling of unconventional Hall conductivity

Next, we obtained conductivities $\sigma_{xy}^{\text{UA}} = \rho_{xy}^{\text{UA}}/(\rho_{xx}^2 + \rho_{xy}^2)$ and $\sigma_{xx} = \rho_{xx}/(\rho_{xx}^2 + \rho_{xy}^2)$, and the magnetic field dependence of both components of the electrical conductivity tensor is shown in Figs. 3(a) and 3(b). At 2 K, the maximum value of the anomalous Hall angle, $\theta_{\text{AH}} = \sigma_{xy}^{\text{UA}}/\sigma_{xx}$, is 0.009 [see Fig. 3(c)], similar to values (≤ 0.01) estimated

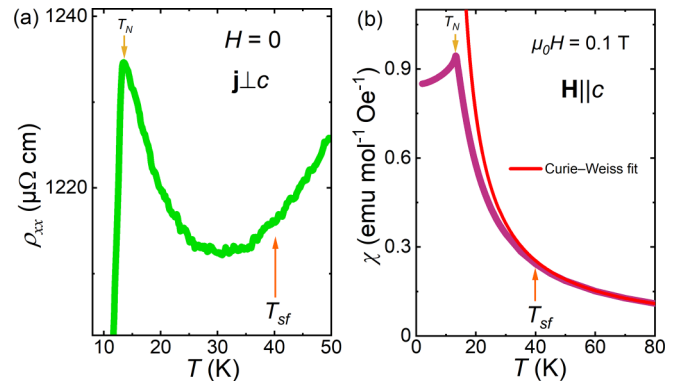


FIG. 2. (a) Temperature-dependent resistivity and (b) magnetic susceptibility, of EuZn₂Sb₂ in the vicinity of T_N . Red line represents fitted Curie-Weiss law (see Supplemental Material [26] for details). T_{sf} denotes the upper-limit temperature for a noticeable effect of spin fluctuations.

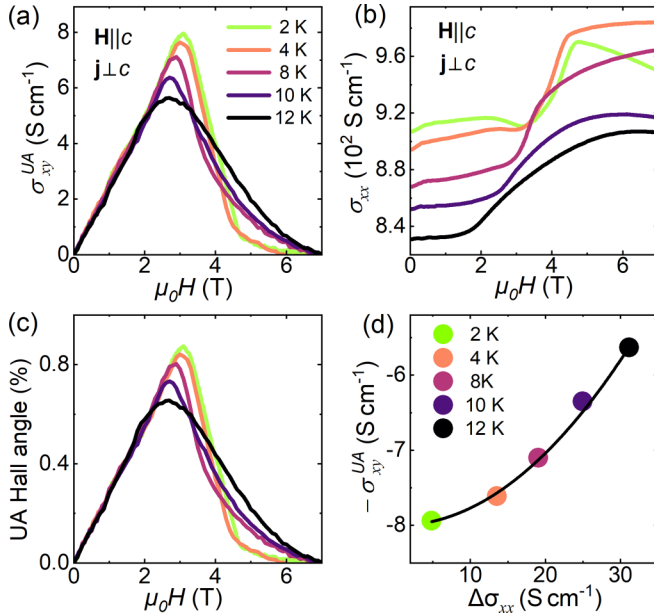


FIG. 3. Magnetic field dependence of (a) unconventional anomalous Hall conductivity σ_{xy}^{UA} , (b) longitudinal conductivity σ_{xx} , and (c) unconventional anomalous Hall angle. (d) Maximum value of σ_{xy}^{UA} at several temperatures, plotted as a function of $\Delta\sigma_{xx}$, and fitted with $\sigma_{xy}^{UA} \propto (\Delta\sigma_{xx})^{1.8 \pm 0.2}$ (black solid line).

for Nd₂(Mo_{1-x}Nb_x)₂O₇ and SrFeO₃, in which scalar spin chirality is held responsible for AHE [29,30]. In the next step, we performed the scaling of the maximum value of anomalous Hall conductivity with the longitudinal conductivity. As only one sample was studied, we used $-\sigma_{xy}^{UA}$ and $\Delta\sigma_{xx}$ values obtained at several different temperatures, where $\Delta\sigma_{xx} = \sigma_{xx}(T, H) - \sigma_{xx}(T, 0)$ [see Fig. 3(d)]. Here, we subtracted the term $\sigma_{xx}(T, 0)$ and used $\Delta\sigma_{xx}$ for scaling because, in this way, we eliminated the contribution from the magnetic disorder-induced scattering, which increases as the temperature rises. Then, we found that $-\sigma_{xy}^{UA}$ is proportional to $(\Delta\sigma_{xx})^{1.8 \pm 0.2}$ [black solid line in Fig. 3(d)]. This relation is close to $\sigma_{xy}^{AH} \propto (\sigma_{xx})^{1.61}$ and $\sigma_{xy}^{AH} \propto (\sigma_{xx})^{1.56}$ obtained for the anomalous Hall conductivity induced by scalar spin chirality and spin-orbit interactions, respectively [30].

It has recently been proposed that vector spin chirality can also bring an anomalous contribution to the Hall effect [24], but it would cancel out in an A-type AFM structure (which is common in the series of compounds that we discuss). This collinear structure in zero magnetic field does not carry finite spin chirality of any kind. Nevertheless, the application of a magnetic field induces spin canting, which results in finite χ_{ijk} , but occurring only within domain walls, as we explain below.

D. Anomalous magnetoresistance

The magnetoresistance, $MR \equiv [\rho_{xx}(H)/\rho_{xx}(0) - 1]$, was measured at several temperatures in a magnetic field applied along the [001] crystallographic direction ($\mathbf{H} \parallel c$). Results are shown in Fig. 1(c). Above T_N , in the entire range of applied magnetic field, MR is negative and monotonically

decreases with increasing magnetic field. As in many materials with large magnetic moments, such MR is mainly due to the reduction of charge carriers' scattering induced by magnetic disorder. At lower temperatures, a shoulder appears in the MR(H) curves (e.g., at ≈ 3 T for 8 K), with position shifting slightly towards stronger magnetic fields as T decreases. Then, for $T \leq 4$ K, the shoulder evolves into a hump at ≈ 3 T, which becomes more pronounced with further decreasing T . Similar anomalies in MR have been reported for EuCd₂As₂, with positions close to the magnetic fields in which the anomalous Hall effect was observed [3,5,7].

When we compared MR(H) curves of EuZn₂Sb₂ with its $M(H)$ isotherms for $\mathbf{H} \parallel c$ [Fig. 1(b)], we noticed no change in the slope of M around fields for which shoulders or humps in MR(H) were observed. This indicates that the origin of these anomalies is not related to any abrupt change in the magnetic structure of EuZn₂Sb₂. On the other hand, at the lowest temperatures, MR(H) stops decreasing in the magnetic field, in which M attains saturation [e.g., $\mu_0 H_{\text{sat}} = 4.7$ T at $T = 2$ K; cf. Fig. 1(b)], and a slight increase of MR is observed with further increasing of the field. Concurrence of the maxima of $\rho_{xy}^{UA}(H)$ and humps of MR(H) through the whole temperature range below T_N strongly indicates that their common origin is spin texture generated by the applied field. In the field range ($< \mu_0 H_{\text{sat}}$) where M changes almost linearly, these maxima occur in fields very close to that, in which spins are canted by $\pi/4$ towards the field direction. This is also the angle of the maximal vector spin chirality resulting from two canted spins (initially antiparallel at zero field). However, vector spin chirality should cancel within a single domain, due to alternating spins in the AFM structure. On the other hand, we noticed that finite χ_{ijk} occurs within domain walls and should be considered as a source of ρ_{xy}^{UA} . EuZn₂Sb₂ has the largest $\mu_0 H_{\text{sat}} = 4.7$ T (at $T = 2$ K, if $\mathbf{H} \parallel c$, or 3.4 T if $\mathbf{H} \perp c$) compared to those of EuCd₂Sb₂, EuCd₂As₂, and EuZn₂As₂: 1.6, 3.2, and 3.6 T, respectively. This indicates the strongest AF interaction and the largest range of field through which the canting of the spins progresses, among the series. The saturation field directly determines the field ($\mu_0 H_{\text{sat}}/\sqrt{2}$), in which modulus of the vector product of two canted spins, $|(\mathbf{S}_j \times \mathbf{S}_k)|$, has a maximum. For EuZn₂Sb₂, at 2 K and in $\mathbf{H} \parallel c$, $\mu_0 H_{\text{sat}}/\sqrt{2}$ is 3.3 T, very close to 3.2 T, where both the local maximum of MR(H) and maximum of $\rho_{xy}^{UA}(H)$ occur [Fig. 1(d)]. Also, when $\mathbf{H} \perp c$, the MR(H) has a maximum [cf. Fig. 4(a)] in such a particular field, $\mu_0 H = 2.4$ T = $(\mu_0 H_{\text{sat}}/\sqrt{2})$. These observations drove our attention to spin chirality as a primary source of maxima in MR and ρ_{xy}^{UA} of EuZn₂Sb₂. Differently from the case of AHE, there was very little discussion about MR resulting from chiral spin textures. Recently, however, this topic has been considered in two theoretical papers [31,32]. They concentrate on spin spirals and skyrmions with spin chiralities similar to those in spin textures, which we propose below.

E. Field-angle-dependent anomalous Hall effect

Figure 5 shows the magnetic-field-dependent Hall resistivity (for $\mathbf{j} \perp c$, $\mathbf{H} \perp \mathbf{j}$) at different field angles from 30° to the 65°, at 2 and 100 K. The anomalous Hall

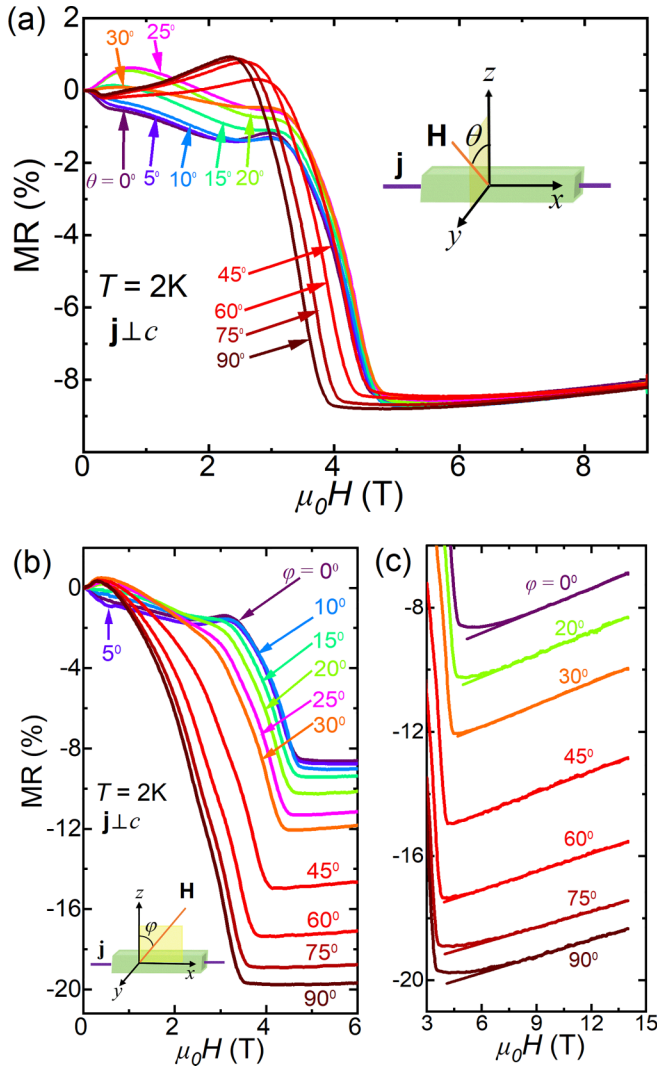


FIG. 4. Magnetoresistance at $T = 2$ K as a function of the magnetic field applied at different angles to the c axis, in two geometries: with angles (a) θ and (b) ϕ , between the c axis and direction of the applied field rotated in a plane $\perp \mathbf{j}$, and from the c axis towards \mathbf{j} , respectively. Insets: The measurement configurations. (c) The extended high-field region of (b), where the MR varies linearly with the field.

contribution was estimated using the relation $\rho_{xy}^{CA} + \rho_{xy}^{UA} = \rho_{xy}(T) - \rho_{xy}^N(100 \text{ K})$. With increasing the angle, the maximum shifts from around 3 T at 30° towards lower fields [see Fig. 5(c)]. A similar shift of the hump in the magnetoresistance data [see Fig. 4(a)]. This corroborates the association of the hump in the magnetoresistance with the unconventional anomalous Hall effect.

F. Mechanism of spin chirality

The trigonal crystal symmetry allows three equivalent anti-ferromagnetic domains, related by 120° rotation (six possible orientations of the spins). Therefore, there are three types of domain walls, between domains, whose spin orientations differ by an azimuthal angle $\Delta\psi = 60^\circ, 120^\circ$, or 180° ,

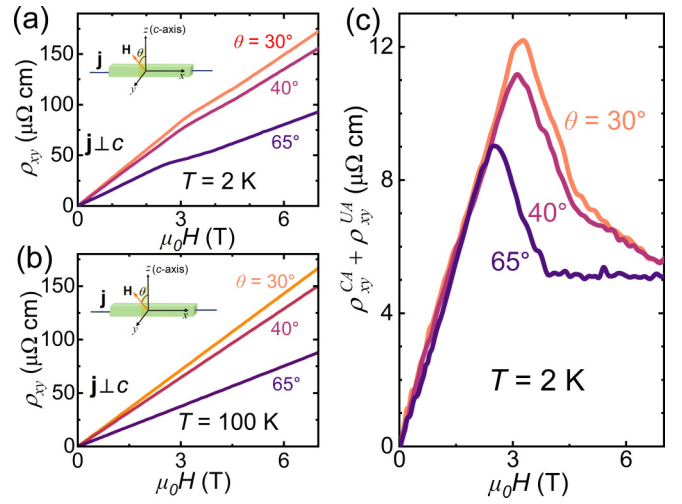


FIG. 5. (a),(b) Magnetic-field-dependent $\rho_{xy}(T)$ for different field angles at $T = 2$ and $T = 100$ K, respectively. (c) Anomalous Hall contribution for different field angles, at $T = 2$ K.

respectively (ψ denotes an arbitrary angle on the plane normal to \mathbf{H} of a projection of the spin on that plane). When a magnetic field is applied along the c axis ($\mathbf{H} \parallel c$), these domains persist. In the field applied transversely to the c axis ($\mathbf{H} \perp c$), the spins quickly (in less than 0.1 T field) undergo a flop transition and only domain walls with $\Delta\psi = 180^\circ$ survive. In both cases, with increasing field, a polar angle (ϑ , between spin and \mathbf{H}) gradually decreases to become zero when all spins align in H_{sat} (sample turns into a single domain). Such domain structures have been observed in EuCd_2As_2 and EuCd_2Sb_2 using resonant x-ray scattering [6,8]. All these domains could be considered as “quasiferromagnetic” domains of collinear spins, ferromagnetically coupled within trigonal layers of Eu^{2+} ions. Of course, charge carriers moving along the ab plane (as in all our magnetotransport measurements) encounter domain walls, which brings additional contributions to MR and Hall resistivity. In the applied field of given strength, the spins within such domain walls have the same ϑ , but their azimuthal angle gradually changes by $\delta\psi$ steps across a domain wall. Therefore, they are noncoplanar and provide finite scalar spin chirality. We sketched an example of such spin texture in Fig. 6. We calculated χ_{ijk} for three spins within a domain wall differing gradually by an arbitrary $\delta\psi$ (from 0 to π range) and having the same ϑ (from 0 to $\pi/2$, which can be mapped to field $H \propto \cos \vartheta$, changing between H_{sat} and zero). The map of χ_{ijk} in $(\vartheta, \delta\psi)$ coordinates is shown in Fig. 7. For the whole range of $\delta\psi$, χ_{ijk} is finite and attains its largest values for ϑ slightly above $\pi/4$, which corresponds to $H = H_{\text{sat}}/\sqrt{2}$.

In EuCd_2As_2 and EuZn_2As_2 , the maxima of ρ_{xy}^{UA} are huge (380, 500, or even $3 \times 10^5 \mu\Omega \text{ cm}$; cf. Table I), but the applied fields in which they occur are weak (0.2 and 0.15 T, respectively); and perhaps the most significant: these maxima are strongest at 9.5 and 20 K, i.e., at, or in the close vicinity of, the respective T_N [3,5,33]. In contrast, the maxima of $\rho_{xy}^{UA}(H)$ in EuZn_2Sb_2 reach only about $10 \mu\Omega \text{ cm}$, but are most prominent at the lowest temperature of 2 K, and in stronger magnetic

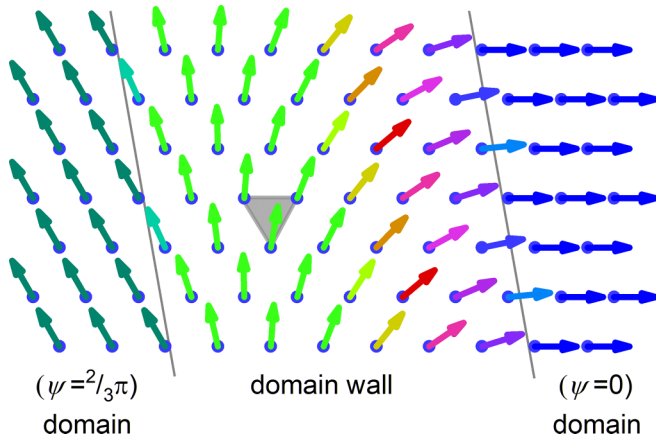


FIG. 6. Spin texture within a domain wall between two domains with spin orientations differing by an azimuthal angle $\Delta\psi = 120^\circ (2/3\pi)$. The applied magnetic field tilts all spins from the ab plane towards the c axis (normal to the page) by the same polar angle ϑ . Every three nearest-neighbor spins (e.g., these of ions spanning the gray triangle) are noncollinear in zero field, and become noncoplanar in the applied magnetic field, which brings out finite scalar spin chirality.

fields ($>2/3H_{\text{sat}}$), this further implies the dominating role of the noncoplanar spin structure, instead of critical spin fluctuations or short-range order.

G. Field-angle-dependent MR

To shed more light on the effect of the applied field on the anomaly in MR, we measured field-angle-dependent magnetoresistance in two geometries. In the first [see Fig. 4(a)],

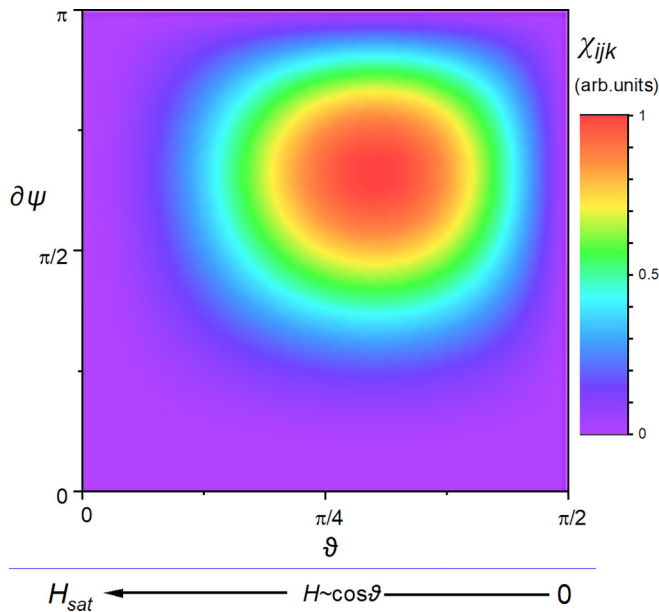


FIG. 7. Map of scalar spin chirality, χ_{ijk} , of three nearest-neighbor spins in the antiferromagnetic domain wall, plotted in $(\vartheta, \delta\psi)$ coordinates. The polar angle of all spins is denoted with ϑ , whereas $\delta\psi$ is the change of the azimuthal angle from spin to spin. The region of maximal χ_{ijk} occurs in fields $H \approx H_{\text{sat}}/\sqrt{2}$.

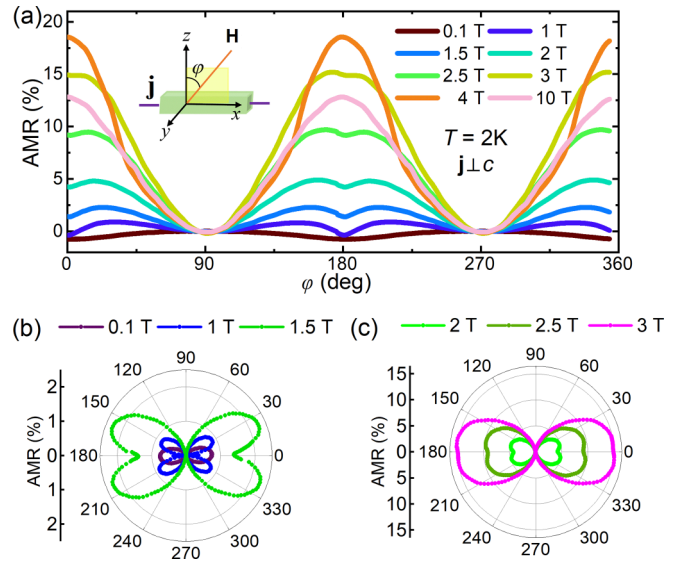


FIG. 8. (a) Angular dependence of the anisotropic magnetoresistance at $T = 2$ K for different magnetic fields. (b),(c) Polar plots of the data shown in (a), separated in two field ranges.

the magnetic field direction was always perpendicular to the current, \mathbf{j} . In the second geometry, the magnetic field direction was gradually changed from transverse ($\mathbf{H} \parallel c \perp \mathbf{j}$, $\phi = 0^\circ$) to longitudinal ($\mathbf{H} \parallel \mathbf{j}$, $\phi = 90^\circ$) to the current [see Fig. 4(b)]. In both cases, MR(H) curves exhibit complex, angle-dependent behavior. The hump in MR(H) at ≈ 3 T (for $\mathbf{H} \parallel c$, and $T = 2$ K), which we associated with the unconventional AHE, in the first geometry, almost does not change its position up to $\theta = 45^\circ$ [Fig. 4(a)], and at larger θ , it shifts to slightly lower magnetic fields (≈ 2.5 T for $\theta = 90^\circ$). This is in good agreement with the changes of anomalous Hall resistivity with the change in θ [see Fig. 5(c)] and simply reflects the decrease of $\mu_0 H_{\text{sat}}$ to 3.7 T (and therefore of $\mu_0 H_{\text{sat}}/\sqrt{2}$ to 2.6 T). In fields above H_{sat} , the curves for all θ collapse on a single one, representing rather typical, weak transverse MR $\propto H^2$. In the second geometry [Fig. 4(b)], when ϕ increases, the position of the hump of MR(H) shifts to lower magnetic fields, but for $\phi \geq 15^\circ$, the hump gradually disappears and turns into a less prominent shoulder. The strong change of MR(H) curves with ϕ is due to the gradual decreasing of H_{sat} (shifting feature related to the spin texture to lower fields) and typical anisotropic magnetoresistance, $\text{AMR} = [\rho(\phi)/\rho_{\parallel}] - 1$, where $\rho_{\parallel} = \rho(\phi = 90^\circ)$, behaving as $\cos 2\phi$ [clearly visible for $\mu_0 H = 10$ T; see Fig. 8(a)]. Evidently, tilting of the direction of the applied magnetic field from transverse to longitudinal to the current is detrimental to the mechanism inducing the hump of MR(H) at $\approx H_{\text{sat}}/\sqrt{2}$ [cf. Fig. 4(b)]. Assuming the scalar spin chirality as an important source of Berry curvature [12], we note that cyclotron movement in the transverse field makes the trajectories of the electrons, their wave functions acquire the geometrical phase factor much more efficiently than electrons in a longitudinal field, moving with almost straight trajectories [34,35]. Therefore, the decay of the anomaly of MR(H) at $\approx H_{\text{sat}}/\sqrt{2}$ observed when the field changes from transverse to longitudinal is another strong

argument in favor of the scalar spin chirality as the principal cause of that anomaly. In fields above H_{sat} , MR varies almost linearly with the H up to the 14 T for all ϕ angles, as shown in Fig. 4(c). The semiclassical MR varies as $\propto H^2$ in low fields and then, at certain fields, saturates to the constant value [36]. Linear MR has been reported many times and most often was attributed to the inhomogeneous mobility caused by disorder [37].

Figure 8(a) shows anisotropic magnetoresistance ($\text{AMR} = [\rho_{xx}(\phi)/\rho_{xx}(90^\circ)] - 1$) recorded at $T = 2$ K and in different magnetic fields. For $H > H_{\text{sat}}$, $\text{AMR}(\phi)$ behaves typically, as $\cos^2 \phi$. For $\mu_0 H = 0.1$ T, AMR exhibits behavior close to $\sin^2 \phi$. In the intermediate range of magnetic fields, the behavior of $\text{AMR}(\phi)$ is more complex, with noticeable local minima at $\phi = 0^\circ$ and 180° . The polar plot of $\text{AMR}(\phi)$ has a butterflylike shape [see Figs. 8(b) and 8(c)]. Similar features in the $\text{AMR}(\phi)$ have been reported for several materials, including ZrSiS [38–40], HoPtBi [41], and BaMn₂Bi₂ [42]. In ZrSiS, it has been ascribed to near-perfect electron-hole compensation [39,40]. For EuZn₂Sb₂, that mechanism is excluded because holes are dominant carriers. However, it is noteworthy that the local minima of the AMR appear in the same field range where spin chirality induces an unconventional anomalous Hall effect.

IV. CONCLUSIONS

We demonstrated the origin of an unconventional anomalous Hall effect and pronounced anomaly in the magnetoresistance in EuZn₂Sb₂, a collinear antiferromagnet with FM arrangement of Eu²⁺ moments in the basal planes, stacked antiferromagnetically along the c axis. This compound exhibits trigonal crystal symmetry, allowing three equivalent antiferromagnetic domains with moments having the azimuthal angle of 60° , 120° , or 180° , respectively. In magnetic fields, spins become canted, inducing scalar spin chirality within the domain walls, having maxima for $H = H_{\text{sat}}/\sqrt{2}$, which corresponds to a polar angle ϑ slightly above $\pi/4$. In the same field range, the large unconventional anomalous Hall and strong anomaly in the MR arise. Furthermore, our field-angle-dependent magnetotransport findings corroborate the conceptualization of spin chirality in this compound.

ACKNOWLEDGMENTS

We acknowledge Dr. T. Romanova for growth of the single crystals. This work was supported by the National Science Centre (NCN, Poland) under Project No. 2021/41/B/ST3/01141 (K.S., D.K., O.P., and P.W.).

-
- [1] H. Su, B. Gong, W. Shi, H. Yang, H. Wang, W. Xia, Z. Yu, P.-J. Guo, J. Wang, L. Ding, L. Xu, X. Li, X. Wang, Z. Zou, N. Yu, Z. Zhu, Y. Chen, Z. Liu, K. Liu, G. Li *et al.*, Magnetic exchange induced Weyl state in a semimetal EuCd₂Sb₂, *APL Mater.* **8**, 011109 (2020).
- [2] Y. Xu, L. Das, J. Z. Ma, C. J. Yi, S. M. Nie, Y. G. Shi, A. Tiwari, S. S. Tsirkin, T. Neupert, M. Medarde, M. Shi, J. Chang, and T. Shang, Unconventional transverse transport above and below the magnetic transition temperature in Weyl semimetal EuCd₂As₂, *Phys. Rev. Lett.* **126**, 076602 (2021).
- [3] X. Cao, J.-X. Yu, P. Leng, C. Yi, X. Chen, Y. Yang, S. Liu, L. Kong, Z. Li, X. Dong, Y. Shi, M. Bibes, R. Peng, J. Zang, and F. Xiu, Giant nonlinear anomalous Hall effect induced by spin-dependent band structure evolution, *Phys. Rev. Res.* **4**, 023100 (2022).
- [4] Z.-C. Wang, E. Been, J. Gaudet, Gadeer Matook A. Alqasseri, K. Fruhling, X. Yao, U. Stuhr, Q. Zhu, Z. Ren, Y. Cui, C. Jia, B. Moritz, S. Chowdhury, T. Devereaux, and F. Tafti, Anisotropy of the magnetic and transport properties of EuZn₂As₂, *Phys. Rev. B* **105**, 165122 (2022).
- [5] E. Yi, D. F. Zheng, F. Pan, H. Zhang, B. Wang, B. Chen, D. Wu, H. Liang, Z. X. Mei, H. Wu, S. A. Yang, P. Cheng, M. Wang, and B. Shen, Topological Hall effect driven by short-range magnetic order in EuZn₂As₂, *Phys. Rev. B* **107**, 035142 (2023).
- [6] J.-R. Soh, C. Donnerer, K. M. Hughes, E. Schierle, E. Weschke, D. Prabhakaran, and A. T. Boothroyd, Magnetic and electronic structure of the layered rare-earth pnictide EuCd₂Sb₂, *Phys. Rev. B* **98**, 064419 (2018).
- [7] J.-R. Soh, F. de Juan, M. G. Vergniory, N. B. M. Schröter, M. C. Rahn, D. Y. Yan, J. Jiang, M. Bristow, P. A. Reiss, J. N. Bland, Y. F. Guo, Y. G. Shi, T. K. Kim, A. McCollam, S. H. Simon, Y. Chen, A. I. Coldea, and A. T. Boothroyd, Ideal Weyl semimetal induced by magnetic exchange, *Phys. Rev. B* **100**, 201102(R) (2019).
- [8] M. C. Rahn, J. R. Soh, S. Francoual, L. S. I. Veiga, J. Stremper, J. Mardegan, D. Y. Yan, Y. F. Guo, Y. G. Shi, and A. T. Boothroyd, Coupling of magnetic order and charge transport in the candidate Dirac semimetal EuCd₂As₂, *Phys. Rev. B* **97**, 214422 (2018).
- [9] F. Weber, A. Cosceev, S. Drobnik, A. Faißt, K. Grube, A. Nateprov, C. Pfleiderer, M. Uhlarz, and H. v. Löhneysen, Low-temperature properties and magnetic order of EuZn₂Sb₂, *Phys. Rev. B* **73**, 014427 (2006).
- [10] J. Blawat, M. Marshall, J. Singleton, E. Feng, H. Cao, W. Xie, and R. Jin, Unusual electrical and magnetic properties in layered EuZn₂As₂, *Adv. Quantum Technol.* **5**, 2200012 (2022).
- [11] R. Karplus and J. M. Luttinger, Hall effect in ferromagnetics, *Phys. Rev.* **95**, 1154 (1954).
- [12] N. Nagaosa, J. Sinova, S. Onoda, A. H. MacDonald, and N. P. Ong, Anomalous Hall effect, *Rev. Mod. Phys.* **82**, 1539 (2010).
- [13] F. D. M. Haldane, Berry curvature on the Fermi surface: Anomalous Hall effect as a topological Fermi-liquid property, *Phys. Rev. Lett.* **93**, 206602 (2004).
- [14] S. Onoda, N. Sugimoto, and N. Nagaosa, Intrinsic versus extrinsic anomalous Hall effect in ferromagnets, *Phys. Rev. Lett.* **97**, 126602 (2006).
- [15] E. Liu, Y. Sun, N. Kumar, L. Muechler, A. Sun, L. Jiao, S.-Y. Yang, D. Liu, A. Liang, Q. Xu, J. Kroder, V. Süß, H. Borrmann, C. Shekhar, Z. Wang, C. Xi, W. Wang, W. Schnelle, S. Wirth, Y. Chen *et al.*, Giant anomalous Hall effect in a ferromagnetic kagome-lattice semimetal, *Nat. Phys.* **14**, 1125 (2018).
- [16] H. Li, B. Zhang, J. Liang, B. Ding, J. Chen, J. Shen, Z. Li, E. Liu, X. Xi, G. Wu, Y. Yao, H. Yang, and W. Wang, Large

- anomalous Hall effect in a hexagonal ferromagnetic Fe_5Sn_3 , *Phys. Rev. B* **101**, 140409(R) (2020).
- [17] S. Yang, Z. Li, C. Lin, C. Yi, Y. Shi, D. Culcer, and Y. Li, Unconventional temperature dependence of the anomalous Hall effect in HgCr_2Se_4 , *Phys. Rev. Lett.* **123**, 096601 (2019).
- [18] H. Ishizuka and N. Nagaosa, Spin chirality induced skew scattering and anomalous Hall effect in chiral magnets, *Sci. Adv.* **4**, eaap9962 (2018).
- [19] M. Uchida, S. Sato, H. Ishizuka, R. Kurihara, T. Nakajima, Y. Nakazawa, M. Ohno, M. Kriener, A. Miyake, K. Ohishi, T. Morikawa, M. S. Bahramy, T.-h. Arima, M. Tokunaga, N. Nagaosa, and M. Kawasaki, Above-ordering-temperature large anomalous Hall effect in a triangular-lattice magnetic semiconductor, *Sci. Adv.* **7**, eabl5381 (2021).
- [20] A. Neubauer, C. Pfleiderer, B. Binz, A. Rosch, R. Ritz, P. G. Niklowitz, and P. Böni, Hall effect in the α phase of MnSi , *Phys. Rev. Lett.* **102**, 186602 (2009).
- [21] N. Kanazawa, Y. Onose, T. Arima, D. Okuyama, K. Ohoyama, S. Wakimoto, K. Kakurai, S. Ishiwata, and Y. Tokura, Large topological Hall effect in a short-period helimagnet MnGe , *Phys. Rev. Lett.* **106**, 156603 (2011).
- [22] C. Sürgers, G. Fischer, P. Winkel, and H. v. Löhneysen, Large topological Hall effect in the non-collinear phase of an antiferromagnet, *Nat. Commun.* **5**, 3400 (2014).
- [23] H. Chen, Q. Niu, and A. H. MacDonald, Anomalous Hall effect arising from noncollinear antiferromagnetism, *Phys. Rev. Lett.* **112**, 017205 (2014).
- [24] J. Kipp, K. Samanta, F. R. Lux, M. Merte, D. Go, J.-P. Hanke, M. Redies, F. Freimuth, S. Blügel, M. Ležaić, and Y. Mokrousov, The chiral Hall effect in canted ferromagnets and antiferromagnets, *Commun. Phys.* **4**, 99 (2021).
- [25] W. J. Kim, J. H. Gruenewald, T. Oh, S. Cheon, B. Kim, O. B. Korneta, H. Cho, D. Lee, Y. Kim, M. Kim, J.-G. Park, B.-J. Yang, A. Seo, and T. W. Noh, Unconventional anomalous Hall effect from antiferromagnetic domain walls of $\text{Nd}_2\text{Ir}_2\text{O}_7$ thin films, *Phys. Rev. B* **98**, 125103 (2018).
- [26] See Supplemental Material at <http://link.aps.org/supplemental/10.1103/PhysRevB.109.125107> for sample characterization (including EDS spectrum, Laue diffractogram, and data on magnetization, heat capacity, and electrical resistivity), and temperature variation of the ordinary and anomalous Hall effect.
- [27] A. F. May, M. A. McGuire, J. Ma, O. Delaire, A. Huq, and R. Custelcean, Properties of single crystalline AZn_2Sb_2 ($A = \text{Ca}, \text{Eu}, \text{Yb}$), *J. Appl. Phys.* **111**, 033708 (2012).
- [28] N. J. Ghimire, A. S. Botana, J. S. Jiang, J. Zhang, Y.-S. Chen, and J. F. Mitchell, Large anomalous Hall effect in the chiral-lattice antiferromagnet CoNb_3S_6 , *Nat. Commun.* **9**, 3280 (2018).
- [29] S. Ishiwata, M. Tokunaga, Y. Kaneko, D. Okuyama, Y. Tokunaga, S. Wakimoto, K. Kakurai, T. Arima, Y. Taguchi, and Y. Tokura, Versatile helimagnetic phases under magnetic fields in cubic perovskite SrFeO_3 , *Phys. Rev. B* **84**, 054427 (2011).
- [30] S. Iguchi, N. Hanasaki, and Y. Tokura, Scaling of anomalous Hall resistivity in $\text{Nd}_2(\text{Mo}_{1-x}\text{Nb}_x)_2\text{O}_7$ with spin chirality, *Phys. Rev. Lett.* **99**, 077202 (2007).
- [31] J. Kipp, F. R. Lux, and Y. Mokrousov, Chiral response of spin-spiral states as the origin of chiral transport fingerprints of spin textures, *Phys. Rev. Res.* **3**, 043155 (2021).
- [32] I. Lima Fernandes, S. Blügel, and S. Lounis, Spin-orbit enabled all-electrical readout of chiral spin-textures, *Nat. Commun.* **13**, 1576 (2022).
- [33] Y. Wang, C. Li, T. Miao, S. S. Zhang, Y. Li, L. Zhou, M. Yang, C. Yin, Y. Cai, C. Song, H. Luo, H. Chen, H. Mao, L. Zhao, H. Deng, Y. Sun, C. Zhu, F. Zhang, F. Yang, Z. Wang *et al.*, Giant and reversible electronic structure evolution in a magnetic topological material EuCd_2As_2 , *Phys. Rev. B* **106**, 085134 (2022).
- [34] M. V. Berry, Quantal phase factors accompanying adiabatic changes, *Proc. R. Soc. London A* **392**, 45 (1984).
- [35] D. Xiao, M.-C. Chang, and Q. Niu, Berry phase effects on electronic properties, *Rev. Mod. Phys.* **82**, 1959 (2010).
- [36] J. Hu and T. F. Rosenbaum, Classical and quantum routes to linear magnetoresistance, *Nat. Mater.* **7**, 697 (2008).
- [37] M. M. Parish and P. B. Littlewood, Non-saturating magnetoresistance in heavily disordered semiconductors, *Nature (London)* **426**, 162 (2003).
- [38] M. N. Ali, L. M. Schoop, C. Garg, J. M. Lippmann, E. Lara, B. Lotsch, and S. S. P. Parkin, Butterfly magnetoresistance, quasi-2d Dirac Fermi surface and topological phase transition in ZrSiS , *Sci. Adv.* **2**, e1601742 (2016).
- [39] J. A. Voerman, L. Mulder, J. C. de Boer, Y. Huang, L. M. Schoop, C. Li, and A. Brinkman, Origin of the butterfly magnetoresistance in ZrSiS , *Phys. Rev. Mater.* **3**, 084203 (2019).
- [40] M. Novak, S. N. Zhang, F. Orbanić, N. Biliškov, G. Eguchi, S. Paschen, A. Kimura, X. X. Wang, T. Osada, K. Uchida, M. Sato, Q. S. Wu, O. V. Yazyev, and I. Kokanović, Highly anisotropic interlayer magnetoresistance in ZrSiS nodal-line Dirac semimetal, *Phys. Rev. B* **100**, 085137 (2019).
- [41] O. Pavlosiuk, P. Fałat, D. Kaczorowski, and P. Wiśniewski, Anomalous Hall effect and negative longitudinal magnetoresistance in half-Heusler topological semimetal candidates TbPtBi and HoPtBi , *APL Mater.* **8**, 111107 (2020).
- [42] K.-K. Huynh, T. Ogasawara, K. Kitahara, Y. Tanabe, S. Y. Matsushita, T. Tahara, T. Kida, M. Hagiwara, D. Arçon, and K. Tanigaki, Negative and positive magnetoresistance in the itinerant antiferromagnet BaMn_2Pn_2 ($\text{Pn} = \text{P}, \text{As}, \text{Sb}, \text{and Bi}$), *Phys. Rev. B* **99**, 195111 (2019).